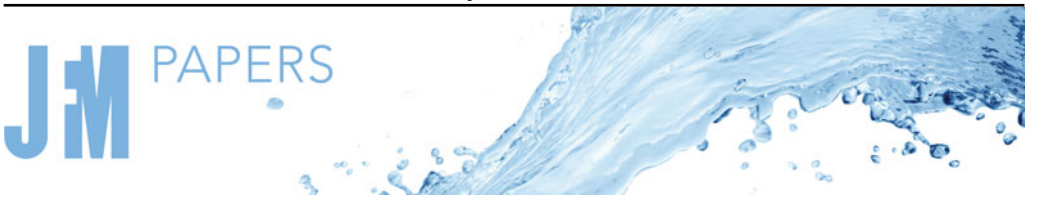
J. Fluid Mech. (2025), *vol.* 1025, A58, doi:10.1017/jfm.2025.10977



Dynamics of poro-viscoelastic wetting with large swelling

Bo Xue Zheng[1,2], **Tak Shing Chan**[1], **Harald van Brummelen**[3] **and Jacco H. Snoeijer**[2]

[1]Mechanics Division, Department of Mathematics, University of Oslo, Oslo 0316, Norway

[2]Physics of Fluids Group, Faculty of Science and Technology, University of Twente, Enschede 7500 AE, The Netherlands

[3]Multiscale Engineering Fluid Dynamics Group, Department of Mechanical Engineering, Eindhoven University of Technology, P.O. Box 513, Eindhoven 5600 MB, The Netherlands

Corresponding authors: Bo Xue Zheng, b.zheng-1@utwente.nl; Tak Shing Chan, taksc@uio.no; Harald van Brummelen, e.h.v.brummelen@tue.nl; Jacco H. Snoeijer, j.h.snoeijer@utwente.nl

(Received 1 July 2025; revised 12 November 2025; accepted 16 November 2025)

The deposition of droplets onto a swollen polymer network induces the formation of a wetting ridge at the contact line. Current models typically consider either viscoelastic effects or poroelastic effects, while polymeric gels often exhibit both properties. In this study, we investigate the growth of the wetting ridge using a comprehensive large-deformation theory that integrates both dissipative mechanisms – viscoelasticity and poroelasticity. In the purely poroelastic case, following an initial instantaneous incompressible deformation, the growth dynamics exhibits scale-free behaviour, independent of the elastocapillary length or system size. A boundary layer of solvent imbibition between the solid surface (in contact with the reservoir) and the region of minimal chemical potential is created. At later times, the ridge equilibrates on the diffusion time scale given by the elastocapillary length. When viscoelastic properties are incorporated, our findings show that, during the early stages (prior to the viscoelastic relaxation time scale), viscoelastic effects dominate the growth dynamics of the ridge and solvent transport is significantly suppressed. Beyond the relaxation time, the late-time dynamics closely resembles that of the purely poroelastic case. These findings are discussed in light of recent experiments, showing how our approach offers a new interpretation framework for wetting of polymer networks of increasing complexity.

Key words: polymers, porous media, drops

© The Author(s), 2025. Published by Cambridge University Press. This is an Open Access article, distributed under the terms of the Creative Commons Attribution licence (https://creativecommons.org/licenses/by/4.0/), which permits unrestricted re-use, distribution and reproduction, provided the original article is properly cited.

https://doi.org/10.1017/jfm.2025.10977 Published online by Cambridge University Press

1. Introduction

The wetting of reticulated polymer networks, such as gels, involves phenomena with far-reaching implications across diverse fields. It plays a significant role in the design of biomimetic materials (Sidorenko, Krupenkin & Aizenberg 2008; Tam *et al.* 2011) and self-healing polymeric materials (Wool & O'connor 1981; Zheng *et al.* 2022). Understanding the influence of capillary forces on solvent transport and hydrogel deformation is crucial for optimising applications such as drug delivery, tissue engineering and soft adhesion systems (Fernández-Barbero *et al.* 2009; Ullah *et al.* 2015; Zhao *et al.* 2018*c*). Additionally, wetting is essential for understanding biophysical processes, including bleb formation in cells (Charras *et al.* 2005), and skin overhydration (Cutting & White 2002). Despite its broad range of applications, contemporary understanding of the physical behaviour of gels in wetting scenarios is still incomplete.

One fundamental wetting scenario involves placing a droplet on a solid surface, offering a model system for both theoretical and experimental studies to address key questions in soft wetting (Carré *et al.* 1996; Pericet-Cámara *et al.* 2008; Jerison *et al.* 2011; Style & Dufresne 2012; Yu 2012; Kajiya *et al.* 2013; Park *et al.* 2014; Style *et al.* 2017; Andreotti & Snoeijer 2020; Khattak *et al.* 2022). When a droplet contacts a soft substrate, capillary forces pull the solid at the contact line to form a wetting ridge (Lester 1961; Rusanov 1975; Carré *et al.* 1996; Pericet-Cámara *et al.* 2008; Pericet-Camara *et al.* 2009; Yu & Zhao 2009; Jerison *et al.* 2011; Limat 2012; Style & Dufresne 2012 ; Yu 2012; Kajiya *et al.* 2013; Style et al. 2013; Lubbers *et al.* 2014; Park *et al.* 2014; Dervaux & Limat 2015; Karpitschka *et al.* 2015; Style *et al.* 2017; Andreotti & Snoeijer 2020; Pandey *et al.* 2020; van Brummelen, Demont & van Zwieten 2021; Chan 2022; Zheng *et al.* 2023; Zheng & Chan 2025). This situation is shown schematically in figure 1(*a*,*b*). While most studies focused on the static-equilibrium properties of the wetting ridge, their dynamical behaviour can be intricate. The growth dynamics of the ridge essentially involves two possible dissipative mechanisms. First, the rearrangement of the polymer chains within the network gives rise to time-dependent elastic properties, with the process characterised by intrinsic viscoelastic relaxation time scales (Carré *et al.* 1996; Long, Ajdari & Leibler 1996; Karpitschka *et al.* 2015; Zhao *et al.* 2018*a*; Andreotti & Snoeijer 2020). Second, polymeric gels can absorb solvent and swell (Zhao *et al.* 2018*b*; Xu *et al.* 2020). The transport of solvent follows a diffusive process characterised by poroelastic time scales. These two dissipation mechanisms – viscoelasticity and poroelasticity – can occur at the same time and are intricately coupled.

Various studies have aimed at unravelling the dynamics of poroelastic gels. Nevertheless, the interpretation of experimental results remains ambiguous. Using a linear model of poroelasticity, Zhao *et al.* (2018*b*) demonstrated that the ridge exhibits logarithmic growth over time. Instead of probing the growth dynamics, Xu *et al.* (2020) investigated the relaxation of an equilibrium ridge upon the removal of the contacting droplet. Their experimental results suggest that the early-time dynamics is dominated by viscoelastic effects, while poroelasticity plays a main role in the late-time behaviour. This conclusion contrasts a study based on atomic force microscopy by Li, Lian & Guan (2023), which suggests that the stress relaxation of hydrogels undergoes a cross-over from short-time poroelastic relaxation to long-time viscoelastic relaxation. Additionally, an alternative investigation of soft-gel dynamics, conducted by Berman *et al.* (2019), focused on the process of adhesive detachment. The authors showed that the early-time relaxation rate is primarily governed by porous flow driven by solid surface stresses. Returning to the context of droplet wetting, recent experimental studies have revealed distinct behaviours of the solvent distribution within the ridge region of a swollen gel.

https://doi.org/10.1017/jfm.2025.10977 Published online by Cambridge University Press

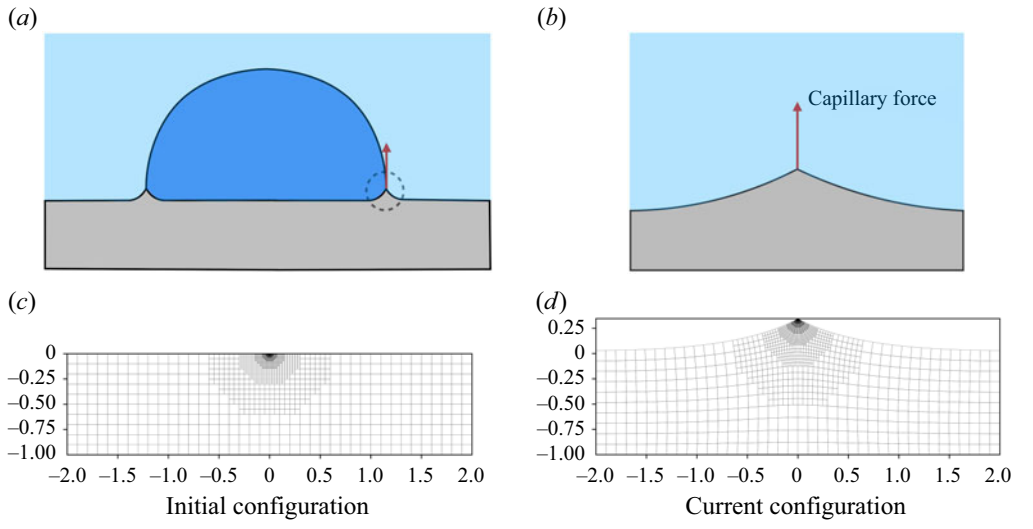


Figure 1. Schematic representation of the physical model. (*a*) Wetting behaviour on a polymeric gel; (*b*) A simplified model illustrating the capillary force acting on the polymeric gel; (*c*) Initial configuration demonstrating the finite-element mesh for a preswollen polymeric gel; (*d*) The mesh configuration of the deformed polymeric gel under the influence of capillary force.

Cai *et al.* (2021) demonstrated that soft polydimethylsiloxane (PDMS) gels phase separate from their solvent in the contact line region. Similar phase separation has also been observed in adhesive contact between a solid bead and a silicone gel substrate (Jensen *et al.* 2015).

The incongruent findings highlight the complex interplay between viscoelastic and poroelastic behaviours in soft gels. Yet, a comprehensive theory that integrates both dissipative mechanisms in wetting scenarios is still lacking. Furthermore, models used to understand ridge dynamics often rely on the assumption of small deformation (Style & Dufresne 2012; Zhao *et al.* 2018*b*), although deformations are large and stresses tend to diverge upon approaching the contact line (Pandey *et al.* 2020). The necessity of using a large-deformation theory was further evidenced by a recent theoretical work by Flapper *et al.* (2023), which reveals a significantly different equilibrium swelling within the wetting ridge compared with results from a linear theory (Zhao *et al.* 2018*b*).

In this study, we develop a theoretical framework to describe the process of ridge formation and capillary-induced solvent transport in polymeric gels with large deformation and significant swelling. We focus on the growth of the elastocapillary ridge on a substrate, after the application of a line force at $t = 0$; see figure 1(*b*). In particular, we address the key question of how this growth is influenced by the competition of viscoelastic and poroelastic dissipation mechanisms. The subsequent sections will be organised as follows: § 2 introduces the formulations for the capillary force-induced gel deformation and solvent-transport system. Section 3 analyses the results for the case in which the solid is a purely poroelastic material (i.e. without viscoelasticity). Section 4 presents the analysis of results that incorporate viscoelastic effects within the system. Finally, conclusions will be drawn in § 5.

2. Poro-visco-elasto-capillary formulation

In this section, we outline the modelling approach used in this paper, which incorporates poroelasticity, viscoelasticity and capillarity. The substrate is modelled using the finite

https://doi.org/10.1017/jfm.2025.10977 Published online by Cambridge University Press

deformation poroelastic model by Hong *et al.* (2008) and Bertrand *et al.* (2016), complemented with a capillary description as in Pandey *et al.* (2020) and Henkel *et al.* (2022). Both descriptions are based on a free-energy formulation, which needs to be complemented with dissipative transport equations. For solvent transport, we adapt a standard diffusive transport model (Hong *et al.* 2008), while we introduce viscoelasticity of the polymer network as an additional dissipative mechanism. This enables us to address the question of whether/when the dynamics is governed by solvent transport or by viscoelastic relaxation. As is common in the study of contact line dynamics, we adopt a two-dimensional description where the action of the contact line is modelled by a line force (figure 1*b*). This reduction reflects that under typical experimental conditions the droplet size is generally much larger than the deformation scale near the contact line (figure 1*a*). Consequently, this allows the use of a plane strain description to formulate the problem.

2.1. *Poro-elastocapillary substrate*

The deformation of the polymer matrix is characterised by a mapping from a reference configuration prior to deformation (i.e. a dry gel without any solvent) to the current state. By standard notation, this mapping is expressed as

$$\boldsymbol{x} = \boldsymbol{\psi}(\boldsymbol{X}, t). \tag{2.1}$$

Here, $\boldsymbol{X}$ represents the position of a material point in the reference domain, which is mapped to its current position $\boldsymbol{x}$ by the deformation map $\boldsymbol{\psi}$. We assume that the geometry is invariant along the contact line, allowing us to treat the problem as two-dimensional (plane strain elasticity). The polymer matrix can be swollen by a solvent, so the mapping $\boldsymbol{\psi}$ does not preserve volume. Defining the deformation gradient tensor as $\boldsymbol{F} = \partial \boldsymbol{x}/\partial \boldsymbol{X}$, the relative change in volume is given by

$$J = \det(\boldsymbol{F}). \tag{2.2}$$

Using the dry network without any solvent as the reference configuration, J naturally defines the 'swelling ratio'. Next, it is assumed that both the polymer molecules that make up the matrix and the solvent molecules are incompressible. This assumption implies that the volumetric change of the network directly determines the local number density of the solvent molecules. Defining $C(\boldsymbol{X}, t)$ as the number of solvent molecules per unit volume in the reference configuration, the molecular incompressibility is ensured by the constraint (Hong *et al.* 2008)

$$J = 1 + \upsilon C, \tag{2.3}$$

where υ is the volume per solvent molecule. The system is thus described by two fields $\boldsymbol{\psi}(\boldsymbol{X}, t)$ and $C(\boldsymbol{X}, t)$, which are constrained by (2.3).

The free energy of the polymer matrix is described using a hyperelastic formulation based on a strain-energy density, $W_{el}(\boldsymbol{F})$, per unit volume in the reference configuration. In the present study, we adopt a common neo-Hookean model based on Gaussian chain elasticity, which for plane-strain conditions gives the energy density

$$W_{el}(\boldsymbol{F}) = \frac{1}{2} G[\boldsymbol{F} : \boldsymbol{F} - 2 - 2\log(\det(\boldsymbol{F}))], \tag{2.4}$$

where G is the shear modulus of the network. The network elasticity is of entropic origin, which can be appreciated from the connection $G = NkT$, where N represents the number of chains per unit volume (Boyce & Arruda 2000; Marckmann & Verron 2006; Hong *et al.* 2008; Kim, Yin & Suo 2022), and kT is the thermal energy. The free energy for the mixing of the solvent and polymer can be described using the Flory–Huggins theory.

https://doi.org/10.1017/jfm.2025.10977 Published online by Cambridge University Press

The corresponding energy density with respect to the volume in the reference configuration takes the form (Hong *et al.* 2008)

$$W_{FH}(C) = -\frac{kT}{v}\left[vC\log\left(1+\frac{1}{vC}\right)+\frac{\chi}{1+vC}\right]. \tag{2.5}$$

The first term represents the entropy of mixing, while the second term is the enthalpy of mixing, the strength of which is set by the interaction parameter χ. The free-energy density for the swollen poroelastic network comprises the sum $W_{el}(\boldsymbol{F}) + W_{FH}(C)$.

Next, we address the capillary contributions. These contributions come in two forms. First, we endow the surface of the substrate with a surface energy γ_s. Adopting the convention that is common in capillarity, this surface free energy is measured per unit area in the current configuration. In principle, this energy can be a function of the degree of swelling at the interface, which would give rise to the Shuttleworth effect (Pandey *et al.* 2020; Henkel *et al.* 2022); for simplicity it is assumed that γ_s is independent of deformation. The second capillary effect is due to the liquid–vapour surface tension γ_{LV}. This can be represented by a localised force (Andreotti & Snoeijer 2020), pulling along the liquid–vapour interface, and leads to the formation of the elasto-capillary ridge, as indicated in figure 1(*b*). Accordingly, we introduce a perfectly localised external traction, characterised by the associated work functional $\mathcal{W}(\boldsymbol{\psi}) = \gamma_{LV}\boldsymbol{t}_{LV}\cdot\boldsymbol{\psi}(\boldsymbol{X}_{cl})$, where $\boldsymbol{X}_{cl}$ denotes the position of the contact line on the solid surface in the reference configuration, and $\boldsymbol{t}_{LV}$ is the pulling direction.

In summary, the functionals describing the free energy of the poro-elastocapillary substrate, and the work performed by the liquid–vapour surface tension, per unit length along the contact line, are given by

$$\mathcal{E}[\boldsymbol{\psi}, C, \Pi] = \int \mathrm{d}^2X\left(W_{el}+W_{FH}+\Pi(1+vC-J)\right)+\int \mathrm{d}s\,\gamma_s, \tag{2.6a}$$

$$\mathcal{W}[\boldsymbol{\psi}] = \gamma_{LV}\boldsymbol{t}_{LV}\cdot\boldsymbol{\psi}(\boldsymbol{X}_{cl}), \tag{2.6b}$$

respectively, where we incorporated the incompressibility constraint (2.3) into the free-energy function via the Lagrange multiplier Π. This Lagrange multiplier turns out to be the osmotic pressure. The integration measure ds represents the arc length in the deformed configuration. We remark that realistic experimental systems can have more intricate energies than assumed here (i.e. beyond neo-Hookean, Flory–Huggins and constant surface tension). However, this does not change the form (2.6*a*), and can in principle be included in the proposed modelling framework. In the Conclusion we return to this point.

In the model that we consider, the poroelastic substrate is contiguous to a liquid reservoir. The absorption of solvent molecules into and deformation of the poroelastic substrate also affect the energy of this liquid reservoir. We assume that during its interaction with the substrate, the liquid reservoir remains at constant pressure, p_0, and chemical potential, μ_0. Accordingly, the deformation of the substrate produces additional energy in the amount of p_0V via work on the reservoir, and the absorption of solvent molecules consumes energy in the amount μ_0N_c, where V and N_c denote the volume of the substrate and the number of solvent molecules it contains, respectively. Noting that $C=(J-1)/v$ by (2.3), the energetic contributions from the interaction of the substrate with the liquid reservoir can be expressed in terms of the deformation and concentration as

$$\begin{aligned} p_0V-\mu_0N_c &= p_0\int \mathrm{d}^2X\,J-\mu_0\int \mathrm{d}^2X\,C \\ &= \tilde{p}_0\int \mathrm{d}^2X\,J+\text{const}, \end{aligned} \tag{2.7}$$

https://doi.org/10.1017/jfm.2025.10977 Published online by Cambridge University Press

with $\tilde{p}_0 = p_0 - \mu_0/v$. The identities in (2.7) convey that, for an incompressible system, an exchange of molecules cannot be distinguished from an exchange of volume. Hence, without loss of generality, we will in the remainder set the chemical potential of the reservoir to $\mu_0 = 0$. For an incompressible system, the value of $\tilde{p}_0$ is without any consequence as well, as it only sets the gauge for the stress. By setting $p_0 = 0$, it is thus understood that we measure the pressure with respect to that of the reservoir. Hence, in the remainder it will suffice to ignore the energetic contributions of the reservoir, under the convention that the gauge of the reservoir is chosen with $\mu_0 = 0$ and $p_0 = 0$.

2.2. *Dynamical equations and dissipation*

We now consider the evolution equations that model the dynamics of wetting ridges in the presence of poroelasticity and viscoelasticity. In modelling the dynamics of poro-viscoelastic materials, it is generally appropriate to neglect inertial effects. Therefore, we consider the momentum balance in quasi-stationary form, and the solvent evolution in time-dependent form.

We present the conservation equation for the solvent in the current configuration. To this end, we denote by $\boldsymbol{v}(\boldsymbol{x}, t) = \partial_t \boldsymbol{\psi}(\boldsymbol{X}, t)$ the material velocity of the substrate, and by $c(\boldsymbol{x}, t) = C(\boldsymbol{X}, t)/J(\boldsymbol{X}, t)$ the solvent concentration in the current configuration, under the deformation in (2.1). Conservation of the solvent is then described by a conservation equation of the form

$$\partial_t c + \boldsymbol{\nabla} \cdot (c\boldsymbol{v}) + \boldsymbol{\nabla} \cdot \boldsymbol{q}_c = 0, \tag{2.8}$$

where $\boldsymbol{\nabla}$ represents the gradient operator in the current configuration and $\boldsymbol{q}_c$ denotes the diffusive flux. To provide a constitutive relation for the diffusive flux, we introduce the chemical potential of the solvent in the reference configuration according to

$$M := \frac{\delta \mathcal{E}}{\delta C} = W'_{FH} + \Pi v, \tag{2.9}$$

where $(\cdot)'$ denotes differentiation. The chemical potential in the current configuration is then given by $\mu(\boldsymbol{x}, t) = M(\boldsymbol{X}, t)$. We define the diffusive flux using Fick's law (corresponding to type I diffusion for very soft polymer networks; Hong *et al.* 2008)

$$\boldsymbol{q}_c = -D\boldsymbol{\nabla}\mu, \tag{2.10}$$

with a constant mobility parameter $D > 0$. The mobility governs the diffusive transport of solvent, and will in the remainder be referred to as a diffusion coefficient. More sophisticated models of the diffusive process can be realised by replacing D with a symmetric-positive-definite tensor $\boldsymbol{D}$, possibly dependent on $\boldsymbol{\psi}$ and C (for example see Bertrand *et al.* 2016).

Neglecting inertial effects in the motion of the substrate, conservation of linear momentum is expressed by the static-equilibrium relation

$$\boldsymbol{\nabla} \cdot \boldsymbol{\sigma} = 0, \tag{2.11}$$

with $\boldsymbol{\sigma}$ the Cauchy stress tensor. We consider constitutive relations for $\boldsymbol{\sigma} = \boldsymbol{\sigma}_{el} + \boldsymbol{\sigma}_v$, that comprise an elastic part $\boldsymbol{\sigma}_{el}$ and (potentially) a viscous part $\boldsymbol{\sigma}_v$. For the considered neo-Hookean hyperelastic material model, the elastic Cauchy stress tensor follows from the free energy as

$$\boldsymbol{\sigma}_{el}(\boldsymbol{x}, t) = \left[J^{-1}\boldsymbol{P} \cdot \boldsymbol{F}^T - \Pi \boldsymbol{I}\right](\boldsymbol{X}, t), \tag{2.12}$$

with $\boldsymbol{P} := \mathrm{d}W_{el}(\boldsymbol{F})/\mathrm{d}\boldsymbol{F}$ as the first Piola–Kirchhoff stress tensor corresponding to the elastic part. Note that we have integrated the pressure part $\Pi \boldsymbol{I}$ originating from the

https://doi.org/10.1017/jfm.2025.10977 Published online by Cambridge University Press

constraint (2.3) into the elastic Cauchy stress. The same Lagrange multiplier Π appears in the chemical potential (2.9), and lies at the origin of the poroelastic coupling. For the viscous part, we adopt a Newtonian stress–strain-rate relation

$$\boldsymbol{\sigma}_v(\boldsymbol{x}, t) = \eta\big(\boldsymbol{\nabla v} + (\boldsymbol{\nabla v})^T\big), \tag{2.13}$$

with $\eta > 0$ as the viscosity. The combined elastic and viscous stress tensors provide a Kelvin–Voigt visco-elastic model.

At the interface between the poroelastic substrate and the liquid reservoir, the traction exerted by the elastic and viscous stresses are balanced by the surface tension. This dynamic interface condition is encoded as

$$\boldsymbol{\sigma} \cdot \boldsymbol{n} = \gamma_s \kappa \boldsymbol{n}, \tag{2.14}$$

where $\boldsymbol{n}$ denotes the exterior unit normal vector and κ denotes the curvature of the interface, under the convention that curvature is negative if the osculating circle is located in the substrate. Condition (2.14) holds everywhere on the interface, except at the contact line, where the interface generally exhibits a kink and, accordingly, the curvature is undefined. A separate, pointwise condition must be specified at the contact line. We impose that the external traction is balanced by the surface-tension tractions acting on both sides of the contact line, according to

$$\gamma_{LV}\boldsymbol{t}_{LV} - \gamma_s(\boldsymbol{t}_- + \boldsymbol{t}_+) = 0, \tag{2.15}$$

where $\boldsymbol{t}_\pm$ are the unit conormal vectors, normal to the contact line, and tangential and external to the smooth parts of the interface adjacent to the contact line. It is noteworthy that (2.15) in fact corresponds to the Neumann law. The conditions (2.14) and (2.15) are naturally satisfied in the equilibrium state (Pandey *et al.* 2020), and imposing them dynamically ensures there is no dissipation associated with capillarity. Likewise, the adjacency of the liquid reservoir implies that the chemical potential at the interface vanishes at equilibrium, and we choose to impose $\mu = 0$ dynamically to avoid any source of dissipation at the interface. This boundary condition implies that the substrate is assumed to be in contact with a solvent reservoir, allowing solvent exchange with the external phase. In terms of figure 1(*a*) this means that in our simulations both the droplet and the surrounding phase can swell the substrate.

The part of the substrate boundary complementary to the interface comprises the bottom and lateral boundaries. We assume that the poroelastic substrate is subjected to a preswelling treatment, in such a manner that the preswelling leads to a homogeneous isotropic expansion of the dry substrate with swelling ratio λ. Subsequently, the bottom boundary is regarded as fixed in the preswollen configuration and, accordingly, we impose $\boldsymbol{\psi}(\boldsymbol{X}, t) = \lambda \boldsymbol{X}$. On the lateral boundaries, we impose free slip in the preswollen configuration, i.e. $\boldsymbol{n} \cdot \boldsymbol{\psi}(\boldsymbol{X}, t) = \boldsymbol{n} \cdot \lambda \boldsymbol{X}$ and $\boldsymbol{n} \times (\boldsymbol{\sigma} \cdot \boldsymbol{n}) \times \boldsymbol{n} = 0$ with $\times$ the cross-product. We regard the bottom and lateral boundaries as closed and therefore set $\boldsymbol{n} \cdot \boldsymbol{\nabla} \mu = 0$.

Our interest pertains to the evolution of the wetting ridge due to a point load at the interface associated with a liquid–vapour interface. We hence regard a preswollen initial configuration corresponding to the equilibrium of the poroelastic substrate in contact with the liquid reservoir, in the absence of the point load. The initial deformation then coincides with that of the preswollen configuration, i.e. $\boldsymbol{\psi}(\boldsymbol{X}, t = 0) = \lambda \boldsymbol{X}$, and the initial concentration is uniform and such that the chemical potential (relative to the liquid reservoir) vanishes.

Thermodynamic consistency, in the sense of dissipation of the formulation without capillarity and without viscoelasticity, was discussed in Hong *et al.* (2008). The effect of $\boldsymbol{\sigma}_v$ can be included in the energy-balance equation as well. Following the steps in

https://doi.org/10.1017/jfm.2025.10977 Published online by Cambridge University Press

Pandey *et al.* (2020) and making use of the dynamical equations (2.8) and (2.11) the free-energy functional evolves according to

$$\mathrm{d}_t(\mathcal{E}-\mathcal{W}) = -\int \mathrm{d}^2x\,\left(2\eta|\nabla \boldsymbol{v}|^2 + D|\nabla\mu|^2\right) + \mathrm{bnd}, \tag{2.16}$$

where $|\nabla \boldsymbol{v}|^2 = \nabla\boldsymbol{v} : \nabla\boldsymbol{v}$ and bnd denotes terms on the part of the boundary of the substrate complementary to the interface; see Appendix B. Equation (2.16) conveys that the free energy is non-increasing, up to work supplied by liquid–vapour surface tension and, possibly, terms on the complementary part of the substrate boundary. Under the aforementioned boundary conditions, however, bnd vanishes so that dissipation only occurs in the bulk of the substrate. Moreover, because equilibrium configurations are characterised by vanishing dissipation, (2.16) conveys that $\boldsymbol{v}$ and μ are uniform in equilibrium. Subject to the aforementioned boundary conditions on the auxiliary part, $\boldsymbol{v} = 0$ and $\mu = 0$ in equilibrium.

2.3. *Weak formulation*

To further elucidate the poro-visco-elastocapillary model, and to provide a basis for the finite-element approximation in § 2.5, we regard the weak formulation of (2.8)–(2.15) constrained by (2.3).

A weak formulation of (2.11) subject to the incompressibility constraint (2.3), including the viscous part (2.13), with interface conditions (2.14) and Neumann law (2.15), can be conveniently expressed in terms of derivatives of the energy and work functionals as

$$\begin{aligned}(\boldsymbol{\psi}(\cdot,t), \Pi(\cdot,t)) : \\ \partial_{\boldsymbol{\psi}}\mathcal{E}[\boldsymbol{\psi}, C, \Pi](\boldsymbol{W}) + \int \mathrm{d}^2x\ \nabla\boldsymbol{w} : \boldsymbol{\sigma}_v \\ +\partial_{\Pi}\mathcal{E}[\boldsymbol{\psi}, C, \Pi](V) = \partial_{\boldsymbol{\psi}}\mathcal{W}[\boldsymbol{\psi}](\boldsymbol{W}) \\ \forall(\boldsymbol{W}, V),\end{aligned} \tag{2.17}$$

where $\partial_{\boldsymbol{\psi}}\mathcal{E}[\boldsymbol{\psi}, C, \Pi](\boldsymbol{W})$ represents the Gateaux derivative of the free-energy functional with respect to its deformation argument in the direction $\boldsymbol{W}$, in particular,

$$\partial_{\boldsymbol{\psi}}\mathcal{E}[\boldsymbol{\psi}, C, \Pi](\boldsymbol{W}) = \frac{\mathrm{d}}{\mathrm{d}s}\mathcal{E}[\boldsymbol{\psi} + s\boldsymbol{W}, C, \Pi]\Big|_{s=0}. \tag{2.18}$$

This notational convention for the Gateaux derivative carries over to other instantiations of $\partial_{(\cdot)}$. The functions $(\boldsymbol{W}, V)$ act as test functions in the reference configuration, while $\boldsymbol{w}(\boldsymbol{x}) = \boldsymbol{W}(\boldsymbol{X})$ is the representation of $\boldsymbol{W}$ in the current configuration. The trial function $(\boldsymbol{\psi}, \Pi)$ and test function $(\boldsymbol{W}, V)$ are supposed to belong to suitable admissibility classes, and $\boldsymbol{\psi}$ and $\boldsymbol{W}$ are subject to conditions at the complementary boundary in accordance with imposed essential boundary conditions. By means of functional derivatives analogous to those in Appendix B, one can show that (2.17) is indeed equivalent to (2.11)–(2.15).

The weak formulation of (2.8) is most conveniently expressed in a form that represents the transport part in the reference configuration and the diffusive part in the current configuration

$$C(\cdot,t): \quad \frac{\mathrm{d}}{\mathrm{d}t}\int \mathrm{d}^2X\ CY + \int \mathrm{d}^2x\ D\nabla\mu\cdot\nabla y = 0 \quad \forall Y, \tag{2.19}$$

with Y as the test function in the reference configuration and $y(\boldsymbol{x}) = Y(\boldsymbol{X})$ its representation in the current configuration; see Appendix C. The definition of the chemical

https://doi.org/10.1017/jfm.2025.10977 Published online by Cambridge University Press

potential in (2.9) is expressed in weak form as

$$M(\cdot, t): \quad \int \mathrm{d}^2 X\, MZ - \partial_C \mathcal{E}[\boldsymbol{\psi}, C, \Pi](Z) = 0 \quad \forall Z, \tag{2.20}$$

where Z acts as test function. The weak formulation of the poro-visco-elastocapillary problem consists of the aggregation of (2.17)–(2.20), equipped with suitable initial conditions for $\boldsymbol{\psi}$ and C.

2.4. *Scales and dimensionless numbers*

The free-energy formulation provides the natural scales for energies and lengths. We start by comparing the Flory–Huggins energy density, scaling with kT/v, to the elastic energy density, scaling with $G = NkT$. Its ratio defines a first dimensionless parameter, Nv. Combined with the Flory–Huggins parameter χ, this determines the natural degree of swelling of the substrate when fully immersed. These parameters are the natural ingredients of the Flory–Rehner theory (Flory & Rehner 1943).

Then, the ratio of surface energy to bulk elastic energy provides a length scale γ_s/G. This defines the so-called elasto-capillary length, which gives a typical measure of elastic deformation. Another length scale of the system is the layer thickness of the preswollen substrate, which we denote as H. The ratio $\gamma_s/(GH)$ geometrically describes the importance of the deformation. A final dimensionless parameter derived from the free energy is obtained from the ratio of surface tensions γ_{LV}/γ_s. This parameter is known to determine the solid angle of the solid, according to Neumann's law (Pandey *et al.* 2020; Flapper *et al.* 2023).

In summary, there are 4 dimensionless numbers governing the 'statics' of the problem. For tractability, we keep them at fixed typical values, namely

$$Nv = 1, \quad \chi = 0, \quad \frac{\gamma_s}{GH} = 1, \quad \frac{\gamma_{LV}}{\gamma_s} = 1. \tag{2.21}$$

Changing the parameter values will lead only to quantitative differences, in particular the degree of preswelling (Nv, χ), the relative size of the elastic deformation (γ_s/GH) and the opening angle of the ridge (γ_{LV}/γ_s). However, our main interest here is to explore the dynamical behaviour of the ridge, which is not expected to change qualitatively with these parameters.

The dynamical model is defined by (2.8) and (2.11), each of which introduces a natural time scale. The equation for solvent transport relates c to μ, which have typical scales $1/v$ and $kT \sim Gv$. To estimate the diffusion time, one can use either γ_s/G (the ridge size) or H (the substrate thickness) as the length scale. We opt for the former to make the equations dimensionless, which introduces the diffusion time scale inside the ridge

$$\tau_D = \frac{(\gamma_s/G)^2}{Dv^2 G} = \frac{\gamma_s^2}{Dv^2 G^3}. \tag{2.22}$$

It should be noticed that the choice of γ_s/G does not imply that it is the only relevant scale. In particular, for thin substrates the thickness H can strongly influence the deformation, especially under fixed-bottom conditions.

In the presence of viscous effects per (2.13), the momentum equation contains a visco-elastic relaxation time scale $\tau_{VE} = \eta/G$, introducing a fifth dimensionless number

$$\tilde{\tau} = \frac{\tau_{VE}}{\tau_D} = \frac{\tau_{VE} D v^2 G^3}{\gamma_s^2}. \tag{2.23}$$

This parameter governs the cross-over from poroelastic to viscoelastic response.

https://doi.org/10.1017/jfm.2025.10977 Published online by Cambridge University Press

In the remainder of the paper we use tildes to denote dimensionless variables. We scale lengths with γ_s/G, energies with vG, while time is scaled with τ_D. Hence, results will be presented in terms of the following dimensionless variables:

$$\tilde{\boldsymbol{x}} = \frac{\boldsymbol{x}}{\gamma_s/G}, \quad \tilde{t} = \frac{t}{\tau_D}, \quad \tilde{\mu} = \frac{\mu}{vG}, \quad \tilde{c} = vc. \tag{2.24}$$

Note that the solvent concentration is made dimensionless with molecular volume (rather than γ_s/G), so that $\tilde{c}$ directly gives the liquid volume fraction.

2.5. *Numerical methods*

We approximate the poro-visco-elastocapillary problem (2.17)–(2.20) by means of the finite-element method in the spatial dependence, and the implicit Euler method in the temporal dependence. The approximation method has been implemented in the open-source software framework Nutils (van Zwieten, van Zwieten & Hoitinga 2022).

To provide adequate resolution at the tip of the wetting ridge, we apply a mesh with *a priori* local refinements near the contact line. Starting with a coarse baseline mesh, we successively subdivide the elements contained in a semi-disc with increasingly small radius, centred at the contact line; see figure 1(*c*). The discrete approximation is obtained by replacing the ambient spaces for the trial functions $\boldsymbol{\psi}$, Π, C, μ and the test functions $\boldsymbol{W}$, V, Y, Z by finite-element spaces subordinate to the locally refined mesh. In particular, we apply continuous piece-wise quadratic approximation spaces for $\boldsymbol{\psi}$, C, μ and $\boldsymbol{W}$, Y, Z and continuous piece-wise linear approximation spaces for Π and V. This implies that for the deformation/pressure pair $(\boldsymbol{\psi}, \Pi)$ we apply so-called Taylor–Hood elements. The functional derivatives that appear in the weak formulation (2.17)–(2.20) are obtained from implementations of the free-energy and work functionals, by means of the automatic differentiation functionality in Nutils.

The nonlinear algebraic problem that emerges in each time step is solved by means of a Newton–Raphson method with line search. The linear tangent problems that occur in each iteration of the Newton–Raphson method are solved by a direct solver. We validate the numerical results by comparing the interface profile at $\tilde{t} = 0^+$ and $\tilde{t} = \infty$ with the equilibrium results presented in Pandey *et al.* (2020) and Flapper *et al.* (2023). Further details are provided in Appendix A, and the code is made available at Zheng *et al.* (2025).

3. Poroelasticity

We first present results for the purely poroelastic model, assuming there is no viscoelastic dissipation. This case corresponds to $\tilde{\tau} = 0$, so that the polymer network adapts instantaneously to the imbibition of the solvent without any effects of viscoelastic relaxation. We recall that we consider the gel to be initially preswollen, equilibrated with the reservoir. For the parameters defined by (2.21), this implies the initial swelling ratio $J_0 = 1.582$. At $\tilde{t} = 0$ we impose a contact line force at the free surface, located at $(\tilde{X}, \tilde{Z}) = (0, 0)$. Since the contact line force pulls vertically upwards, the contact line position remains at $\tilde{x} = 0$ in the deformed configuration.

3.1. *Ridge growth*

To illustrate the evolution of the free surface of the poroelastic gel, figure 2(*a*) plots the vertical displacement of the free surface, $\tilde{u}_z(\tilde{x}, \tilde{t})$, versus the horizontal position in the deformed configuration, $\tilde{x}$, at various instants, $\tilde{t}$. At $\tilde{t} = 0$, the polymeric gel surface is flat, corresponding to the homogeneously preswollen initial state. Upon application of the capillary force at the contact line, the gel exhibits an instantaneous response, as

https://doi.org/10.1017/jfm.2025.10977 Published online by Cambridge University Press

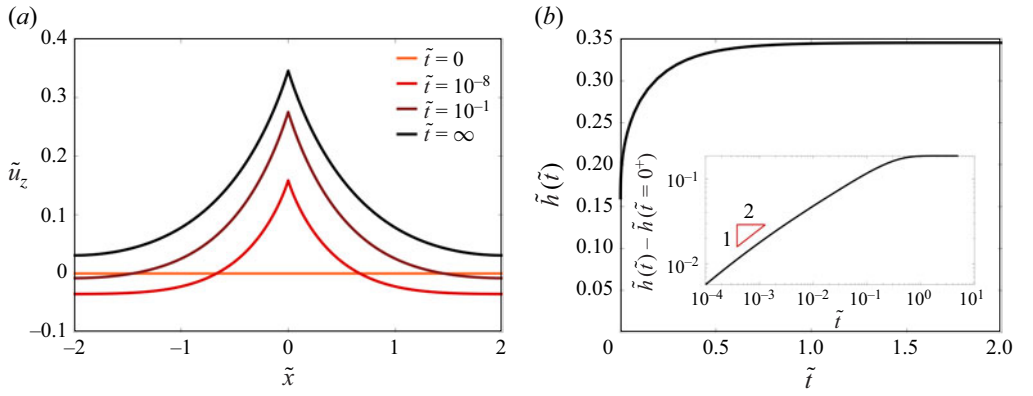


Figure 2. (*a*) Time-dependent profiles of the free surface of the purely poroelastic substrate ($\tilde{\tau}=0$) after the application of a line force at $\tilde{t}=0$; (*b*) The ridge height $\tilde{h}$ as a function of time. Inset: evolution of the ridge height $\tilde{h}(\tilde{t})-\tilde{h}(0^+)$ after the instantaneous response, on a logarithmic scale.

evidenced by the profile at $\tilde{t}=10^{-8}$. We refer to this very early time limit as $\tilde{t}=0^+$. This instantaneous response is essentially incompressible because the solvent within the gel did not yet have any time to diffuse, preventing any noticeable change in swelling immediately after the capillary force is applied; see also Zhao *et al.* (2018*b*). Note that an instantaneous response would in reality be prevented by inertia, but this involves extremely small time scales. (Inertia acts on a time scale that can be estimated from the elastocapillary length and the speed of elastic waves, as $(\gamma_s/G)/\sqrt{G/\rho}=\gamma_s\rho^{1/2}/G^{3/2}$, typically of the order of 10^{-5} s for soft gels. Formally, this inertial transient precedes the viscoelastic and poroelastic regimes of interest, which is of the order of seconds or larger.) Subsequently, as time progresses, the gel absorbs solvent from the surroundings and swells, resulting in an increase in its volume, as indicated by the curve at $\tilde{t}=10^{-1}$ and the profile at $\tilde{t}=\infty$, in figure 2(*a*). The substrate eventually reaches an equilibrium state as $\tilde{t}\to\infty$.

To further characterise the dynamics of the ridge growth, we show the height of the elastocapillary ridge, $\tilde{h}(\tilde{t}):=\tilde{u}_z(0,\tilde{t})$, as a function of time in figure 2(*b*). We indeed observe an instantaneous displacement at $\tilde{t}=0^+$, which is followed by a gradual increase until equilibrium is reached. The inset of figure 2(*b*) presents the same data, but instead plots $\tilde{h}(\tilde{t})-\tilde{h}(0^+)$ versus $\tilde{t}$ on a logarithmic scale. This graph shows that after the instantaneous incompressible response, the growth of the ridge follows a power law with an exponent of 1/2. In dimensional terms, this growth implies that $h(t)-h(0^+)\sim(Dv^2Gt)^{1/2}$, which is scale free in the sense that it does not involve the elasto-capillary length γ_s/G nor the system size H. This scale-free behaviour reflects that the growth is initially due to diffusive imbibition of the solvent into the substrate. After this scaling regime, the equilibration is observed around $\tilde{t}\sim 1$, suggesting that the diffusion time scale τ_D, is indeed the appropriate poroelastic time scale for the late-time process, where the ridge size γ_s/G begins to play a role.

3.2. *Chemical potential*

Solvent transport plays a fundamental role in the dynamics of the wetting-ridge formation. The chemical potential μ per (2.9) effectively controls the magnitude and direction of the solvent flux, because the flux is proportional to $-\nabla\mu$. Hence, the spatio-temporal evolution of μ provides meaningful insight into the underlying solvent-transport mechanisms.

https://doi.org/10.1017/jfm.2025.10977 Published online by Cambridge University Press

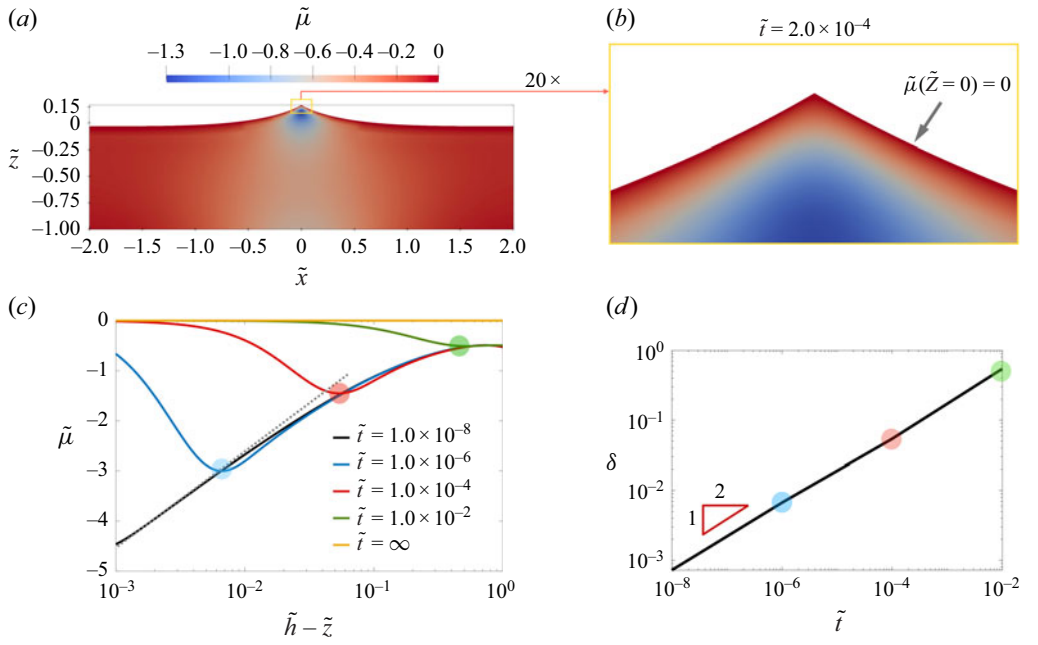


Figure 3. Spatio-temporal evolution of the chemical potential for a poroelastic substrate ($\tilde{\tau} = 0$). (*a*) The rescaled chemical potential field at $\tilde{t} = 2 \times 10^{-4}$; (*b*) A zoomed-in view near the contact line position from (*a*); (*c*) Measurement of $\tilde{\mu}$ from the tip along the z-direction at different times. The circles indicating the local minima define the boundary layer thickness δ. The dashed line indicates the prediction (3.1) for the instantaneous incompressible response; (*d*) Boundary layer thickness δ as a function of time $\tilde{t}$.

Figure 3(*a*) presents the rescaled chemical potential $\tilde{\mu}$ in the porous substrate, at $\tilde{t} = 2 \times 10^{-4}$. The figure conveys that the chemical potential displays a localised minimum just below the contact line, represented in the figure by the blue region. This minimum in the chemical potential can equivalently be interpreted as a region of low 'pore pressure', and originates from the tensile elastic stress generated by the deformed polymer network. The solvent thus tends to diffuse towards this blue region. A magnified view near the contact line is given in figure 3(*b*). This zoom shows that $\tilde{\mu} = 0$ at the free surface, reflecting the boundary condition that the surface is in equilibrium with the reservoir. The blue region is separated from the free surface by a thin boundary layer, that gives rise to a strong local gradient of $\tilde{\mu}$. Hence, the solvent flux will be strongest near the interface, so that the predominant flux is from the reservoir into the ridge.

Next, we focus on the temporal evolution of the chemical potential. Figure 3(*c*) shows $\tilde{\mu}$ along the vertical line below the contact line ($\tilde{x} = 0$), at different times. The horizontal axis $\tilde{h} - \tilde{z}$ represents the distance to the contact line. The graphs confirm the appearance of a minimum of $\tilde{\mu}$, which shifts and fades over time. At very long times $\tilde{\mu} \to 0$ everywhere, corresponding to the global equilibration. Interestingly, the data for early times ($\tilde{t} = 10^{-8}$, shown in black) seem to follow a logarithmic dependence $\tilde{\mu} \sim \ln(\tilde{h} - \tilde{z})$. This logarithmic behaviour can be understood in terms of the instantaneous incompressible response expected at $t = 0^{+}$. At this early-time limit, the concentration field did not yet have time to evolve, and the chemical potential, as defined in (2.9), follows the behaviour of Π. For an incompressible corner, Π plays the role of the pressure that is known to exhibit a logarithmic dependence on the distance to the contact line (Pandey *et al.* 2020). Translated in terms of the scaled chemical potential, this takes the form

https://doi.org/10.1017/jfm.2025.10977 Published online by Cambridge University Press

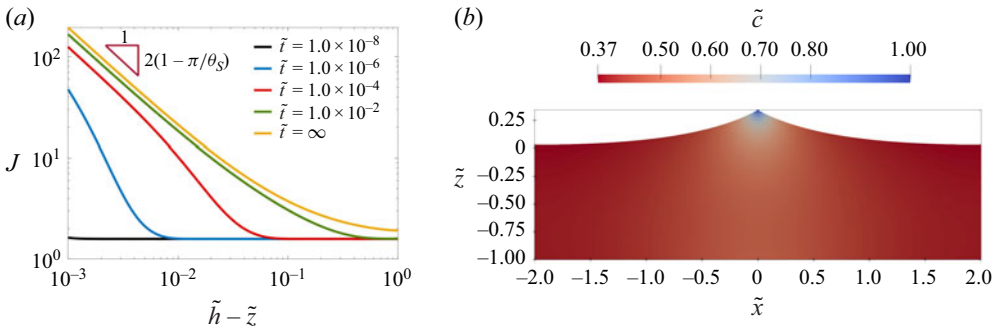


Figure 4. Swelling dynamics for a poroelastic substrate ($\tilde{\tau}=0$). (*a*) Measurement of J from the tip along the z-direction at different times. The preswelling at $t=0$ corresponds to an initial $J_0=1.582$. (*b*) Solvent volume fraction field $\tilde{c}$ at the final equilibrium state. Near the tip the solvent fraction $\tilde{c}\to 1$, while at large distance one recovers the value due to preswelling $\tilde{c}\approx 0.37$.

$$\tilde{\mu}\simeq\left(\frac{\pi}{\theta_S}-\frac{\theta_S}{\pi}\right)\ln(\tilde{r}), \tag{3.1}$$

where $\tilde{r}$ is the distance to the contact line and θ_S is the corner angle ($\theta_S=2\pi/3$ when $\gamma_{LV}/\gamma_s=1$). This prediction is superimposed as the grey dashed line in figure 3(*c*), and indeed perfectly captures the observed behaviour in the vicinity of the contact line at $\tilde{t}=10^{-8}$. Note that the logarithmic divergence of $\tilde{\mu}$ is not specific to the neo-Hookean solid; a different constitutive relation only modifies the prefactor in (3.1).

The picture that emerges is that the instantaneous response dictates that the chemical potential diverges logarithmically, according to (3.1), in the vicinity of the contact line. This behaviour, however, is incompatible with the boundary condition $\mu=0$ that is imposed at the free surface. This conundrum is resolved by the emergence of a thin boundary layer near the contact line. Indeed, the blue and red curves in figure 3(*c*) closely follow the near-instantaneous response (black line) away from the contact line. At shorter distances, the logarithmic trend is not followed, and the data tend to $\tilde{\mu}=0$ at the contact line. We estimate the size of the boundary layer δ by tracing the minimum of the chemical potential, indicated by the circles. Figure 3(*d*) reports the boundary layer thickness over time, which again follows a diffusive $1/2$ scaling. Hence, we associate the dynamics of the boundary layer with the scale-free diffusive solvent transport.

3.3. *Swelling dynamics*

From the previous results we thus conclude that the incompressible response gives an excellent representation of the behaviour at early times, except for a narrow boundary layer $\delta\sim t^{1/2}$. Swelling does occur in this boundary layer, which is characterised by a strong flux $\sim 1/\delta\sim 1/t^{1/2}$. Now we turn to the question of how this translates to the spatio-temporal dynamics of the swelling inside the substrate.

Figure 4(*a*) shows the swelling ratio J as a function of the vertical distance $\tilde{h}-\tilde{z}$, measured directly below the contact line. The initial value corresponds to the preswollen substrate with $J_0=1.582$. In line with the evolution of the boundary layer for $\tilde{\mu}$, we observe that swelling is initiated close to the contact line, and gradually invades the entire domain. The long-time equilibrium profile is given by the yellow line. The strongest swelling occurs at the tip of the wetting ridge, and exhibits a power-law singularity. Indeed, previous work on the equilibrium state (Flapper *et al.* 2023) has analytically demonstrated that, for the neo-Hookean solid, the swelling ratio $J\sim\tilde{r}^{\beta}$, where the exponent $\beta=2(1-\pi/\theta_S)$; in this expression θ_S once again is the opening angle of the tip

https://doi.org/10.1017/jfm.2025.10977 Published online by Cambridge University Press

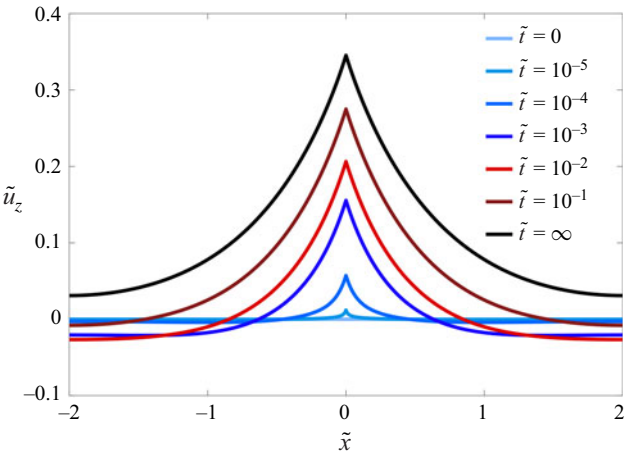


Figure 5. Time-dependent surface profile for a visco-poroelastic substrate ($\tilde{\tau} = 10^{-3}$), after the application of a line force at $\tilde{t} = 0$. For $\tilde{t} < \tilde{\tau}$, a small ridge emerges gradually from the substrate with a viscoelastic dynamics. For $\tilde{t} > \tilde{\tau}$, the profiles closely follow the purely poroelastic dynamics of figure 2(*a*).

of the solid. The numerical results closely follow this analytical prediction, also transiently in the vicinity of the contact line.

The divergence of J implies that the tip region is almost purely liquid. Specifically, the scaled concentration $\tilde{c} = 1 - 1/J$ directly gives the liquid volume fraction. The volume fraction at equilibrium is shown in figure 4(*b*), and indeed approaches unity near the tip. In the present formulation the liquid cannot phase separate between the matrix and the liquid reservoir, as observed in some experiments (Jensen *et al.* 2015; Cai *et al.* 2021; Hauer *et al.* 2023). It is clear, however, that the strong aspiration of liquid in elastic corners provides a natural mechanism for this phenomenon.

4. Visco-poroelasticity

We now turn to the complete model, including the effect of viscoelasticity. This case corresponds to $\tilde{\tau} = \tau_{VE}/\tau_D \neq 0$, for which there is a competition of two time scales: the poroelastic diffusive time scale τ_D and the viscoelastic time scale τ_{VE} reflecting the relaxation of the polymer network.

4.1. *Ridge growth*

Figure 5 depicts a typical visco-poroelastic evolution of the free surface for the case where $\tilde{\tau} = 10^{-3}$. This value of $\tilde{\tau}$ implies that the network relaxation is faster compared with the diffusive transport of the solvent. Nonetheless, we observe that the growth of the ridge is fundamentally altered with respect to the purely poroelastic case: the instantaneous incompressible response is now replaced by a gradual viscoelastic growth of the wetting ridge, occurring on the time scale $\tilde{t} < \tilde{\tau}$. The ridge emerges gradually in this regime, both in terms of its height and its width. It is noteworthy that the solid angle of the ridge forms instantaneously, in accordance with the Neumann law (2.15), which is implicit in (2.17) as a natural (weakly imposed) condition; see also Karpitschka *et al.* (2015) and Chan (2022). We note that, after $\tilde{t} \approx \tilde{\tau} = 10^{-3}$ (dark blue), the profiles closely follow those in figure 2(*a*). The limiting transport mechanism during this late-time dynamics is the slow poroelastic solvent flow, not the viscoelastic relaxation.

To further quantify the ridge dynamics, we report in figure 6(*a*) the height of the ridge $\tilde{h}$ as a function of time $\tilde{t}$ in a semi-log plot, for various viscoelastic relaxation times $\tilde{\tau}$.

https://doi.org/10.1017/jfm.2025.10977 Published online by Cambridge University Press

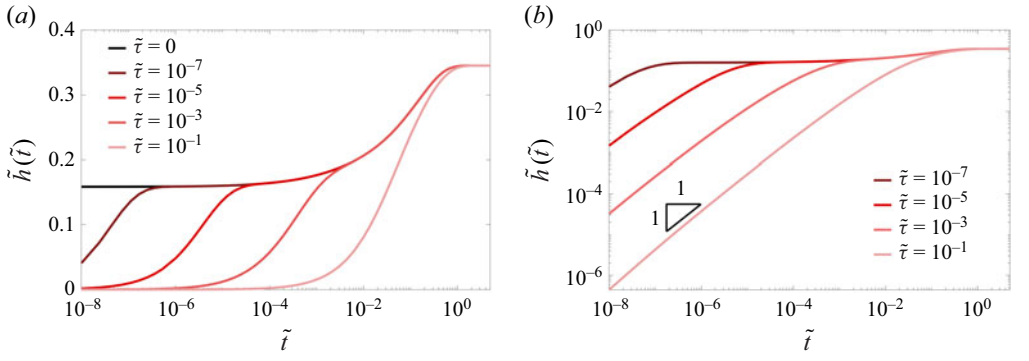


Figure 6. Growth of the ridge for visco-poroelastic substrates. (*a*) The deformation $\tilde{h}$ of the tip as a function of time $\tilde{t}$ for various viscoelastic relaxation times $\tilde{\tau}$. (*b*) Same data on a double logarithmic scale, showing the linear ridge growth when viscoelasticity is included.

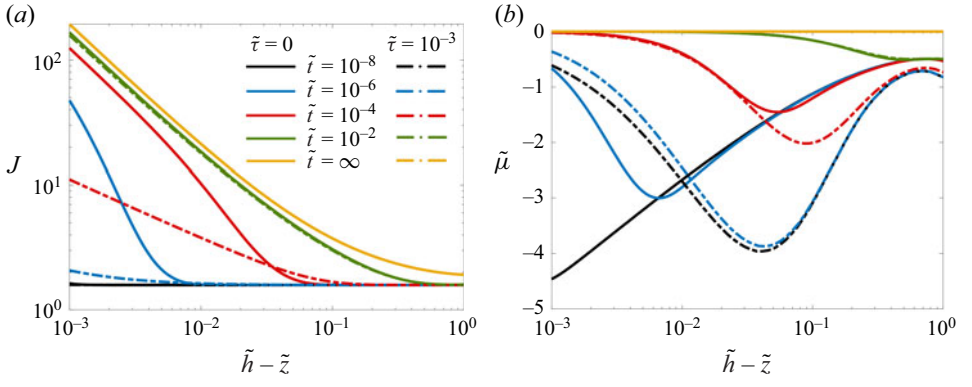


Figure 7. Swelling ratio (*a*) and chemical potential (*b*), for a visco-poroelastic substrate. Profiles along the z-direction from the tip. The solid lines correspond to a purely poroelastic material ($\tilde{\tau} = 0$). The dashed lines correspond to a visco-poroelastic material with $\tilde{\tau} = 10^{-3}$.

When $\tilde{\tau} = 0$ (represented by the black line), we recover the purely poroelastic case that we previously observed to exhibit an instantaneous response. Conversely, when $\tilde{\tau}$ is non-zero, one no longer observes this instantaneous deformation. Instead, the tip height grows gradually until joining the purely poroelastic curve approximately when $\tilde{t} \sim \tilde{\tau}$. These results confirm the cross-over, from viscoelastic at early times to poroelastic at later times. Figure 6(*b*) shows the same data on a doubly logarithmic plot. We find a linear initial growth in the viscoelastic regime. The scaling follows $\tilde{h} \sim \tilde{t}/\tilde{\tau}$, which in dimensional units amounts to $h \sim \gamma_s t/(G\tau_{VE})$. Bearing in mind that the network viscosity $\eta = G\tau_{VE}$, the growth of the ridge is dictated by the capillary velocity γ_s/η. Hence, the linear ridge growth here arises from the Newtonian rheology employed in the viscoelastic term of the model. Note that if the network instead followed a nonlinear relaxation (e.g. a power-law rheology), the early-time scaling of the ridge height would be modified accordingly, and take over the rheological exponent.

4.2. *Swelling dynamics*

Next, we turn to the transport of solvent in the presence of viscoelasticity. Figure 7(*a*) shows the swelling ratio below the contact line, at different times. The dash-dotted lines represent the results for the case where $\tilde{\tau} = 10^{-3}$, which was previously considered

https://doi.org/10.1017/jfm.2025.10977 Published online by Cambridge University Press

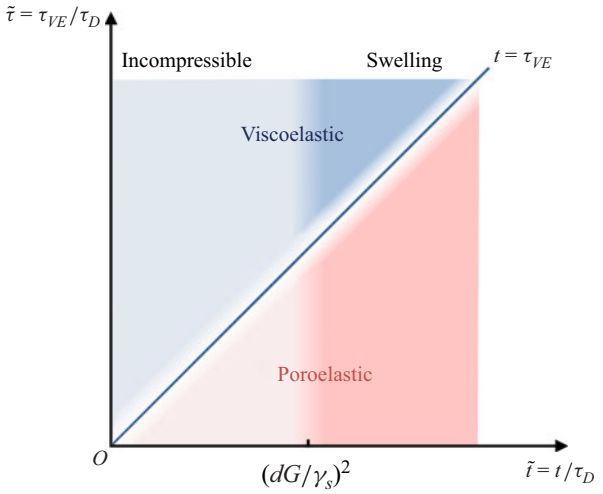


Figure 8. Regime map illustrating the interplay between the viscoelastic and poroelastic dynamics. For a given $\tilde{\tau}$, the initial response is viscoelastic followed by a poroelastic regime. In the latter regime, the response can initially be incompressible depending on the dimensionless distance to the contact line ($\tilde{d} = dG/\gamma_s$).

in figure 5. To clearly illustrate how viscoelasticity changes the transport dynamics, we also report the purely poroelastic results for $\tilde{\tau} = 0$, as solid lines. For times $\tilde{t} > \tilde{\tau}$, the solid lines and dash-dotted lines essentially overlap. This implies that the late-time swelling dynamics is not affected by viscoelasticity, but is purely poroelastic in nature. By contrast, large differences are observed for the early time dynamics, $\tilde{t} < \tilde{\tau}$. There is still a tendency towards swelling near the tip, even at very short times, but this swelling is retarded compared with the purely poroelastic case. The suppression of solvent transport at early times can be attributed to the vanishing of logarithmic divergence in the chemical potential, as shown in figure 7(*b*). In other words, the viscoelastic stresses inhibit the development of strong 'pore pressure'. Only when $\tilde{t} \geq \tilde{\tau}$ do the curves for $\tilde{\tau} = 0$ and $\tilde{\tau} \neq 0$ start to overlap, indicating the regime where transport is purely poroelastic.

To summarise the dynamical regimes, figure 8 presents a schematic diagram in terms of the normalised time $\tilde{t} = t/\tau_D$ and the ratio $\tilde{\tau} = \tau_{VE}/\tau_D$. The temporal evolution of the simulation crosses the different regimes in the diagram along a horizontal line, at a given value of $\tilde{\tau}$. The gel initially behaves as an incompressible viscoelastic solid, since no solvent influx occurs in regions far from the tip. As time progresses and solvent diffusion penetrates the bulk, the substrate gradually enters the poroelastic regime, leading to swelling at larger scales. At a distance d from the contact line, the onset of swelling is governed by the diffusive time $\tilde{t} \sim (dG/\gamma_s)^2$. The cross-over line $\tilde{t} = \tilde{\tau}$ delineates the transition between viscoelastic- and poroelastic-dominated behaviour.

5. Conclusion and remarks

In this study, we investigate the deformation and solvent transport within a poro-viscoelastic polymeric gel under the influence of capillary forces. A large-deformation model is employed to accurately characterise the polymeric gel's deformation, while the Flory–Huggins theory is utilised to describe the mixing energy between the solvent and the polymeric gel. We assume a non-inertial motion for the system and incorporate viscoelasticity to describe the polymeric gel's complex behaviour.

https://doi.org/10.1017/jfm.2025.10977 Published online by Cambridge University Press

We begin by examining purely poroelastic substrates, where viscoelastic effects are absent. When a capillary force is applied at the contact line, the substrate responds instantaneously as an incompressible material, resulting in immediate deformation at $\tilde{t} = 0^+$. Subsequently, the substrate exhibits poroelastic behaviour, reflected in the swelling and the growth of the ridge. The increase in the tip's height over time follows a power law with an exponent of 1/2, implying that the early-time dynamics is scale free and independent of the elastocapillary length. This result appears to be at variance with the study by Zhao *et al.* (2018*b*), who investigated the ridge growth for an axisymmetric droplet using a linear elasticity theory. The authors report an instantaneous response, similar to our observations, but they describe the subsequent dynamics as following a logarithmic relation in the time range $\tau_D \ll t \ll (RG/\gamma_s)^2\tau_D$, where R is the droplet radius. We suspect the dynamics in Zhao *et al.* (2018*b*) is, in fact, governed by a $t^{1/2}$ scaling at very early times, with the logarithmic behaviour emerging as an intermediate asymptotic regime specific to the axisymmetric case.

Regarding solvent transport, we observe a logarithmic singularity in the chemical potential at the tip at $\tilde{t} = 0^+$. This singularity is regularised by a thin boundary layer, characterised by a large solvent flux from the adjacent liquid reservoir into the substrate near the tip. Over time, the minimum in chemical potential is found to move away from the tip into the substrate, driving the gradual swelling of the ridge into the substrate. Additionally, the swelling ratio exhibits a singularity at the contact line, indicating that the volume fraction of the solvent approaches unity near the tip. The relationship between the swelling ratio and the distance from the tip can be described by a power law with an exponent of $2(1 - \pi/\theta_S)$, in line with previous predictions for the equilibrium case (Flapper *et al.* 2023). This contrasts with previous results for small deformations (Zhao *et al.* 2018*b*), for which a logarithmic divergence of the swelling ratio has been predicted.

The incorporation of viscoelastic effects in the substrate reveals that viscoelasticity dominates the early time dynamics of the ridge growth (prior to the relaxation time) and significantly suppresses solvent transport. Beyond the viscoelastic relaxation time, the dynamics converges to that of the purely poroelastic case.

Finally, let us discuss the interpretation of recent experiments in light of our findings. First, we remark that our results are consistent with the experimental results of Xu *et al.* (2020), which examined the relaxation of an equilibrium ridge. Specifically, the early-time dynamics is dominated by viscoelastic effects, while poroelasticity becomes the primary factor governing the late-time behaviour. However, the reversed scenario was proposed in Li *et al.* (2023), who measured the force relaxation using atomic force microscopy after pressing an indenter into the hydrogel. These experiments exhibited a slow decay of the measured force at long times, which was attributed to viscoelasticity. These experiments were conducted on agarose gels, which might be susceptible to plastic reconfigurations that manifest themselves as long-time creep. The present model describes reversible stress relaxation in chemically cross-linked gels. In such materials, the rearrangement of polymer chains within the network is reversible: the permanent cross-links ensure that the reference configuration can be fully recovered once the external load is removed. In contrast, physically cross-linked gels such as the agarose used by Li *et al.* (2023) may experience bond breakage and reformation, leading to irreversible changes in the reference state. Such plastic deformations lie outside the scope of the current model, which assumes that the reference configuration remains well defined and recoverable. Clearly, this kind of material would require a different class of viscoelastic models compared with what was used in our simulations. When staying within the realm of linear viscoelasticity, a long-time relaxation scenario would require a vanishing stress relaxation function, with no resultant elasticity at large times.

https://doi.org/10.1017/jfm.2025.10977 Published online by Cambridge University Press

The focus of the paper was to identify the relevant dynamical mechanisms and scaling laws for poro-viscoelastic wetting. A natural extension of the work would be a systematic exploration of the parameters of the model. For example, we have kept the parameters $Nv = 1$ and $\chi = 0$, which should be realistic for a PDMS network swollen by uncross-linked chains. A hydrogel would typically correspond to much smaller values of Nv and variable χ, giving rise to much stronger preswelling ratios. Varying γ_s/GH would e.g. be of interest to investigate very thin substrates. Similarly, one can estimate realistic experimental values for the poroelastic and viscoelastic time scales. Experiments on PDMS and on hydrogels involve τ_D from seconds to hours, depending on the specific material and the relevant length scales (Hu *et al.* 2011; Chan *et al.* 2012), with the viscoelastic time scale typically much smaller in magnitude (Chan *et al.* 2012). For poroelastic wetting of PDMS, τ_D is found to be of the order of seconds while the viscoelastic scale is reported as $\tau_{VE} \sim 0.1$ s. (Xu *et al.* 2020). This range of $\tilde{\tau} = \tau_D/\tau_{VE} \ll 1$ was indeed the focus of our simulations.

When moving to a fully quantitative description of experiments, one might have to go beyond neo-Hookean elasticity, Flory–Huggins energy and Kelvin–Voigt viscoelasticity. In principle, however, each of these refinements can be incorporated in the proposed modelling framework, by adjusting the free energy in (2.6*a*) or modifying the transport coefficients. For example, one might anticipate that the coefficients χ, G, D and γ_s exhibit a dependence on the local volume fraction $\tilde{c}$ (Schott 1992; Emerson *et al.* 2013; Bertrand *et al.* 2016; Pandey *et al.* 2020). This is of particular interest near the tip, where $\tilde{c} \to 1$. In this case the diffusion is expected to be much faster (Schott 1992; Bertrand *et al.* 2016). Still, the invasion of solvent though the boundary layer is still expected to follow $t^{1/2}$, with a diffusion coefficient corresponding to that of the preswollen substrate. In this context, an interesting question is how surface tension evolves at large volume fraction, as this affects the angle θ_S at the tip of the ridge, and would lead to Marangoni-like shear stresses (Pandey *et al.* 2020). Another point for future exploration is the effect of the boundary condition. Here, we assumed that both the drop and the surrounding fluid can swell the substrate. Experimentally, one can envision scenarios where only one (or none) of these phases can enter the substrate, which will modify the details of the ridge growth. Note that within the model one can also change the boundary condition via the type of forcing that is imposed; for instance, an oscillatory shear force would mimic a standard rheological characterisation used in experiments.

After these considerations, we emphasise that our theoretical results reveal the mechanism by which solvent is transported to the wetting ridge. This offers a route that could explain the experimentally observed extraction of solvent at the contact line (Cai *et al.* 2021), and shows the potential of the presented modelling approach.

Acknowledgements. B.X.Z. and T.S.C. gratefully acknowledge the financial support from the Research Council of Norway (project no. 315110). J.H.S. acknowledges support from NWO through VICI grant no. 680-47-632. This research was partly conducted within the Industrial Partnership Program *Fundamental Fluid Dynamics Challenges in Inkjet Printing* (*FIP*), a joint research program of Canon Production Printing, Eindhoven University of Technology, University of Twente, Utrecht University and the Netherlands Organization for Scientific Research (NWO). E.H.v.B. gratefully acknowledges financial support through the FIP program. All simulations have been performed using the open source software package Nutils (www.nutils.org). B.X.Z. would also like to extend heartfelt gratitude to Dr G.v. Zwieten and Dr M.H. Essink for their valuable insights and assistance with coding.

Funding. Open access funding provided by University of Twente.

Declaration of interests. The authors report no conflict of interest.

Data availability statement. The data that support the findings of this study are openly available in [Zenodo] at https://doi.org/10.5281/zenodo.17516418.

https://doi.org/10.1017/jfm.2025.10977 Published online by Cambridge University Press

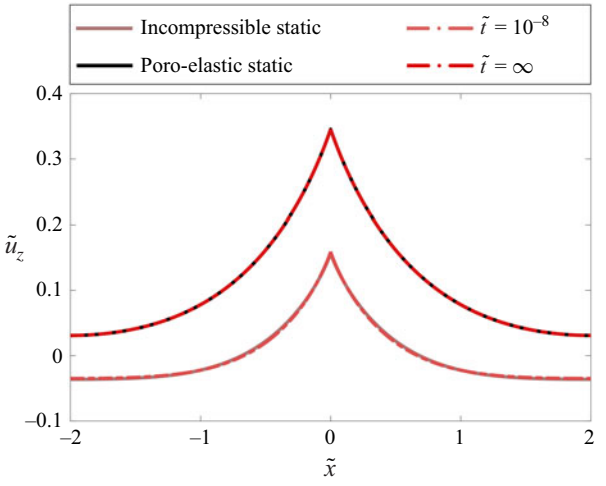


Figure 9. Comparison of dynamic and static wettability profiles on the polymeric gel. The profiles at early time ($\tilde{t} = 10^{-8}$) and late time ($\tilde{t} = \infty$, equilibrium) are compared with static wettability results for incompressible and poroelastic materials, respectively.

Appendix A. Validation

We validate our computations by comparing the dynamic results obtained in this study with previous static findings related to wetting on incompressible and poroelastic substrates. As analysed previously, at $t = 0^+$, the substrate behaves as an incompressible material. Given that we are considering quasi-static motion in the present case, the deformation of the substrate at $t = 0^+$ should align with the static wetting behaviour observed on an incompressible substrate. In the equilibrium state ($t = \infty$), the substrate profile is expected to converge with the static wetting results for a poroelastic material. The profiles of the substrate surface from prior studies on wetting in incompressible substrates (Pandey *et al.* 2020) and poroelastic substrates (Flapper *et al.* 2023) have been plotted and compared with the present results for dynamic wetting on the poroelastic substrate in figure 9. The agreement serves as a validation of our time-dependent numerical solutions.

Appendix B. Dissipation

To derive the dissipation relation (2.16), we first note that

$$\begin{aligned} \mathrm{d}_t \mathcal{E}[\boldsymbol{\psi}, C, \Pi] = &\int \mathrm{d}^2 X \, (\mathrm{d}_{\boldsymbol{F}} W_{el} - \Pi \, \mathrm{d}_{\boldsymbol{F}} J) : \partial_t \boldsymbol{F} \\ &+ \int \mathrm{d}^2 X \, (W'_{FH}(C) + \Pi v) \partial_t C \\ &+ \int \mathrm{d}^2 X \, (1 + vC - J) \, \partial_t \Pi \\ &+ \mathrm{d}_t \int \mathrm{d}s \, \gamma_s . \end{aligned} \tag{B1}$$

By virtue of the static-equilibrium condition and the partition $\boldsymbol{\sigma} = \boldsymbol{\sigma}_{el} + \boldsymbol{\sigma}_v$, via standard transformations and integration-by-part identities we obtain for the first term

https://doi.org/10.1017/jfm.2025.10977 Published online by Cambridge University Press

$$\begin{aligned}\int \mathrm{d}^2X\ (\mathrm{d}_{\boldsymbol{F}} W_{el} - \Pi\, \mathrm{d}_{\boldsymbol{F}} J) : \partial_t \boldsymbol{F} \\ = \int \mathrm{d}^2x\ \boldsymbol{\sigma}_{el} : \boldsymbol{\nabla v} + \int \mathrm{d}^2x\ \boldsymbol{v} \cdot (\boldsymbol{\nabla} \cdot \boldsymbol{\sigma}) \\ = \int \mathrm{d}s\ \boldsymbol{v} \cdot \boldsymbol{\sigma} \cdot \boldsymbol{n} - \int \mathrm{d}^2x\ \boldsymbol{\sigma}_v : \boldsymbol{\nabla v}.\end{aligned} \tag{B2}$$

Note that the second term in the second line of (B2) in fact vanishes per (2.11). For the second term in (B1), it follows from (2.8), the Reynolds transport theorem and the divergence theorem that

$$\begin{aligned}\int \mathrm{d}^2X\ (W'_{FH}(C) + \Pi v)\, \partial_t C = \int \mathrm{d}^2X\ M \partial_t C \\ = \int \mathrm{d}^2x\ \mu\big(\partial_t c + \boldsymbol{\nabla} \cdot (c\boldsymbol{v})\big) \\ = \int \mathrm{d}^2x\ \boldsymbol{\nabla}\mu \cdot \boldsymbol{q}_c - \int \mathrm{d}s\ \mu\, \boldsymbol{q}_c \cdot \boldsymbol{n}.\end{aligned} \tag{B3}$$

The third term in (B1) vanishes on account of the constraint (2.3). For the fourth term, standard shape-calculus identities (see e.g. van Brummelen *et al.* 2017) lead to

$$\mathrm{d}_t \int \mathrm{d}s\ \gamma_s = -\int \mathrm{d}s\ \gamma_s\, \kappa\ \boldsymbol{v} \cdot \boldsymbol{n} + \gamma_s\, (\boldsymbol{t}_- + \boldsymbol{t}_+) \cdot \boldsymbol{v}(\boldsymbol{x}_{cl}). \tag{B4}$$

It is to be noted that the surface integral in the first term extends across the smooth parts of the interface on either side of the contact line.

For the work functional (2.6*b*), it holds that

$$\mathrm{d}_t \mathcal{W}[\boldsymbol{\psi}] = \gamma_{LV} \boldsymbol{t}_{LV} \cdot \partial_t \boldsymbol{\psi}(\boldsymbol{X}_{cl}) = \gamma_{LV} \boldsymbol{t}_{LV} \cdot \boldsymbol{v}(\boldsymbol{x}_{cl}). \tag{B5}$$

The final expression in (B5) follows from transporting the penultimate expression from the reference configuration to the current configuration.

Collecting the results in (B1)–(B5), one obtains

$$\begin{aligned}\mathrm{d}_t(\mathcal{E} - \mathcal{W}) = -\int \mathrm{d}^2x\ \boldsymbol{\sigma}_v : \boldsymbol{\nabla v} + \int \mathrm{d}^2x\ \boldsymbol{\nabla}\mu \cdot \boldsymbol{q}_c \\ + \int \mathrm{d}s\ \boldsymbol{v} \cdot (\boldsymbol{\sigma} \cdot \boldsymbol{n} - \gamma_s \kappa \boldsymbol{n}) - \int \mathrm{d}s\ \mu\, \boldsymbol{q}_c \cdot \boldsymbol{n} \\ + \big(\gamma_s\, (\boldsymbol{t}_- + \boldsymbol{t}_+) - \gamma_{LV} \boldsymbol{t}_{LV}\big) \cdot \boldsymbol{v}(\boldsymbol{x}_{cl}).\end{aligned} \tag{B6}$$

The dissipation relation (2.16) follows by introducing the constitutive relations (2.10) and (2.13), the dynamic interface condition (2.14), the homogeneous Dirichlet condition for the chemical potential at the interface and the Neumann law (2.15).

Appendix C. Weak formulation (2.19)

To derive the weak formulation (2.19) from the conservation (2.8), we first multiply (2.8) with test function $y(\boldsymbol{x})$ and integrate on the poroelastic substrate in the current configuration

$$\int \mathrm{d}^2x\ y\big(\partial_t c + \boldsymbol{\nabla} \cdot (c\boldsymbol{v}) - \boldsymbol{\nabla} \cdot D\boldsymbol{\nabla}\mu\big) = 0, \tag{C1}$$

https://doi.org/10.1017/jfm.2025.10977 Published online by Cambridge University Press

where we introduced the constitutive relation (2.10). By virtue of the Reynolds transport theorem, it holds that

$$\int \mathrm{d}^2x\; y\big(\partial_t c + \boldsymbol{\nabla}\cdot(c\boldsymbol{v})\big) = \frac{\mathrm{d}}{\mathrm{d}t}\int \mathrm{d}^2x\; yc. \tag{C2}$$

Noting that $c(\boldsymbol{x},t) = C(\boldsymbol{X},t)/J(\boldsymbol{X},t)$, pull-back of the right-hand side of (C2) to the reference configuration leads to

$$\frac{\mathrm{d}}{\mathrm{d}t}\int \mathrm{d}^2x\; yc = \frac{\mathrm{d}}{\mathrm{d}t}\int \mathrm{d}^2X\; YC. \tag{C3}$$

Applying integration-by-parts to the right-most term in parentheses in (C1), it follows that

$$\frac{\mathrm{d}}{\mathrm{d}t}\int \mathrm{d}^2X\; CY + \int \mathrm{d}^2x\; D\boldsymbol{\nabla}\mu\cdot\boldsymbol{\nabla}y + \int \mathrm{d}s\; y\,\boldsymbol{n}\cdot(D\boldsymbol{\nabla}\mu) = 0. \tag{C4}$$

On parts of the boundary of the poroelastic substrate where μ is subject to Dirichlet conditions, e.g. at the interface, the test function y is required to vanish. The complementary part of the boundary is assumed to be impermeable and, hence, the homogeneous Neumann condition $\boldsymbol{n}\cdot(D\boldsymbol{\nabla}\mu) = 0$ holds. Accordingly, the boundary integral in (C4) vanishes, and one obtains (2.19).

References

Andreotti, B. & Snoeijer, J.H. 2020 Statics and dynamics of soft wetting. *Annu. Rev. Fluid Mech.* **52** (1), 285–308.

Berman, J.D., Randeria, M., Style, R.W., Xu, Q., Nichols, J.R., Duncan, A.J., Loewenberg, M., Dufresne, E.R. & Jensen, K.E. 2019 Singular dynamics in the failure of soft adhesive contacts. *Soft Matt.* **15** (6), 1327–1334.

Bertrand, T., Peixinho, J., Mukhopadhyay, S. & MacMinn, C.W. 2016 Dynamics of swelling and drying in a spherical gel. *Phys. Rev. Appl.* **6** (6), 064010.

Boyce, M.C. & Arruda, E.M. 2000 Constitutive models of rubber elasticity: a review. *Rubber Chem. Technol.* **73** (3), 504–523.

van Brummelen, E.H., Demont, T.H.B. & van Zwieten, G.J. 2021 An adaptive isogeometric analysis approach to elasto-capillary fluid-solid interaction. *Intl J. Numer. Meth. Engng* **122** (19), 5331–5352.

Cai, Z., Skabeev, A., Morozova, S. & Pham, J.T. 2021 Fluid separation and network deformation in wetting of soft and swollen surfaces. *Commun. Mater.* **2** (1), 21.

Carré, A., Gastel, J.-C. & Shanahan, M.E.R. 1996 Viscoelastic effects in the spreading of liquids. *Nature* **379** (6564), 432–434.

Chan, E.P., Deeyaa, B., Johnson, P.M. & Stafford, C.M. 2012 Poroelastic relaxation of polymer-loaded hydrogels. *Soft Matt.* **8** (31), 8234–8240.

Chan, T.S. 2022 The growth and the decay of a visco-elastocapillary ridge by localized forces. *Soft Matt.* **18** (38), 7280–7290.

Charras, G.T., Yarrow, J.C., Horton, M.A., Mahadevan, L. & Mitchison, T.J. 2005 Non-equilibration of hydrostatic pressure in blebbing cells. *Nature* **435** (7040), 365–369.

Cutting, K.F. & White, R.J. 2002 Maceration of the skin and wound bed 1: its nature and causes. *J. Wound Care* **11** (7), 275–278.

Dervaux, J. & Limat, L. 2015 Contact lines on soft solids with uniform surface tension: analytical solutions and double transition for increasing deformability. *Proc. R. Soc. A Math. Phys. Engng Sci.* **471** (2176), 20140813.

Emerson, J.A., Toolan, D.T.W., Howse, J.R., Furst, E.M. & Epps III , T.H. 2013 Determination of solvent–polymer and polymer–polymer Flory–Huggins interaction parameters for poly (3-hexylthiophene) via solvent vapor swelling. *Macromolecules* **46** (16), 6533–6540.

Fernández-Barbero, A., Suárez, I.J., Sierra-Martín, B., Fernández-Nieves, A., de las Nieves, F.J., Marquez, M., Rubio-Retama, J. & López-Cabarcos, E. 2009 Gels and microgels for nanotechnological applications. *Adv. Colloid Interface Sci.* **147–148**, 88–108.

Flapper, M.M., Pandey, A., Essink, M.H., Van Brummelen, E.H., Karpitschka, S. & Snoeijer, J.H. 2023 Reversal of solvent migration in poroelastic folds. *Phys. Rev. Lett.* **130** (22), 228201.

Flory, P.J. & Rehner, J. 1943 Statistical mechanics of cross-linked polymer networks I. Rubberlike elasticity. *J. Chem. Phys.* **11** (11), 512–520.

https://doi.org/10.1017/jfm.2025.10977 Published online by Cambridge University Press

HAUER, L., CAI, Z., SKABEEV, A., VOLLMER, D. & PHAM, J.T. 2023 Phase separation in wetting ridges of sliding drops on soft and swollen surfaces. *Phys. Rev. Lett.* **130** (5), 058205.

HENKEL, C., ESSINK, M.H., HOANG, T., VAN ZWIETEN, G.J., VAN BRUMMELEN, E.H., THIELE, U. & SNOEIJER, J.H. 2022 Soft wetting with (a) symmetric shuttleworth effect. *Proc. R. Soc. A* **478** (2264), 20220132.

HONG, W., ZHAO, X., ZHOU, J. & SUO, Z. 2008 A theory of coupled diffusion and large deformation in polymeric gels. *J. Mech. Phys. Solids* **56** (5), 1779–1793.

HU, Y., CHEN, X., WHITESIDES, G.M., VLASSAK, J.J. & SUO, Z. 2011 Indentation of polydimethylsiloxane submerged in organic solvents. *J. Mater. Res.* **26** (6), 785–795.

JENSEN, K.E., SARFATI, R., STYLE, R.W., BOLTYANSKIY, R., CHAKRABARTI, A., CHAUDHURY, M.K. & DUFRESNE, E.R. 2015 Wetting and phase separation in soft adhesion. *Proc. Natl Acad. Sci. USA* **112** (47), 14490–14494.

JERISON, E.R., XU, Y., WILEN, L.A. & DUFRESNE, E.R. 2011 Deformation of an elastic substrate by a three-phase contact line. *Phys. Rev. Lett.* **106** (18), 1–4.

KAJIYA, T., DAERR, A., NARITA, T., ROYON, L., LEQUEUX, F. & LIMAT, L. 2013 Advancing liquid contact line on visco-elastic gel substrates: stick-slip vs. continuous motions. *Soft Matt.* **9** (2), 454–461.

KARPITSCHKA, S., DAS, S., VAN GORCUM, M., PERRIN, H., ANDREOTTI, B. & SNOEIJER, J.H. 2015 Droplets move over viscoelastic substrates by surfing a ridge. *Nat. Commun.* **6** (1), 7891.

KHATTAK, H.K., KARPITSCHKA, S., SNOEIJER, J.H. & DALNOKI-VERESS, K. 2022 Direct force measurement of microscopic droplets pulled along soft surfaces. *Nat. Commun.* **13** (1), 4436.

KIM, J., YIN, T. & SUO, Z. 2022 Polyacrylamide hydrogels. V. Some strands in a polymer network bear loads, but all strands contribute to swelling. *J. Mech. Phys. Solids* **168**, 105017.

LESTER, G.R. 1961 Contact angles of liquids at deformable solid surfaces. *J. Colloid Sci.* **16** (4), 315–326.

LI, H., LIAN, X. & GUAN, D. 2023 Crossover behavior in stress relaxations of poroelastic and viscoelastic dominant hydrogels. *Soft Matt.* **19** (29), 5443–5451.

LIMAT, L. 2012 Straight contact lines on a soft, incompressible solid. *Eur. Phys. J. E* **35** (12), 1–13.

LONG, D., AJDARI, A. & LEIBLER, L. 1996 Static and dynamic wetting properties of thin rubber films. *Langmuir* **12** (21), 5221–5230.

LUBBERS, L.A., WEIJS, J.H., BOTTO, L., DAS, S., ANDREOTTI, B. & SNOEIJER, J.H. 2014 Drops on soft solids: free energy and double transition of contact angles. *J. Fluid Mech.* **747**, R1.

MARCKMANN, G. & VERRON, E. 2006 Comparison of hyperelastic models for rubber-like materials. *Rubber Chem. Technol.* **79** (5), 835–858.

PANDEY, A., ANDREOTTI, B., KARPITSCHKA, S., VAN ZWIETEN, G.J., VAN BRUMMELEN, E.H. & SNOEIJER, J.H. 2020 Singular nature of the elastocapillary ridge. *Phys. Rev. X* **10** (3), 031067.

PARK, S.J., WEON, B.M., LEE, J.S., LEE, J., KIM, J. & JE, J.H. 2014 Visualization of asymmetric wetting ridges on soft solids with X-ray microscopy. *Nat. Commun.* **5** (1), 4369.

PERICET-CAMARA, R., AUERNHAMMER, G.K., KOYNOV, K., LORENZONI, S., RAITERI, R. & BONACCURSO, E. 2009 Solid-supported thin elastomer films deformed by microdrops. *Soft Matt.* **5** (19), 3611–3617.

PERICET-CÁMARA, R., BEST, A., BUTT, H.J. & BONACCURSO, E. 2008 Effect of capillary pressure and surface tension on the deformation of elastic surfaces by sessile liquid microdrops: an experimental investigation. *Langmuir* **24** (19), 10565–10568.

RUSANOV, A.I. 1975 Theory of wetting of elastically deformed bodies, 1. Deformation with a finite contact-angle. *Colloid J. USSR* **37** (4), 614–622.

SCHOTT, H. 1992 Swelling kinetics of polymers. *J. Macromol. Sci. B: Phys.* **31** (1), 1–9.

SIDORENKO, A., KRUPENKIN, T. & AIZENBERG, J. 2008 Controlled switching of the wetting behavior of biomimetic surfaces with hydrogel-supported nanostructures. *J. Mater. Chem.* **18** (32), 3841–3846.

STYLE, R.W., BOLTYANSKIY, R., CHE, Y., WETTLAUFER, J.S., WILEN, L.A. & DUFRESNE, E.R. 2013 Universal deformation of soft substrates near a contact line and the direct measurement of solid surface stresses. *Phys. Rev. Lett.* **110** (6), 066103.

STYLE, R.W. & DUFRESNE, E.R. 2012 Static wetting on deformable substrates, from liquids to soft solids. *Soft Matt.* **8** (27), 7177–7184.

STYLE, R.W., JAGOTA, A., HUI, C.Y. & DUFRESNE, E.R. 2017 Elastocapillarity: surface tension and the mechanics of soft solids. *Annu. Rev. Condens. Matt. Phys.* **8**, 99–118.

TAM, S.K., DUSSEAULT, J., BILODEAU, S., LANGLOIS, G., HALLÉ, J.-P. & YAHIA, L'.H. 2011 Factors influencing alginate gel biocompatibility. *J. Biomed. Mater. Res. A* **98** (1), 40–52.

ULLAH, F., OTHMAN, M.B.H., JAVED, F., AHMAD, Z. & AKIL, H.M. 2015 Classification, processing and application of hydrogels: a review. *Mater. Sci. Engng C* **57**, 414–433.

https://doi.org/10.1017/jfm.2025.10977 Published online by Cambridge University Press

VAN BRUMMELEN, E.H., SHOKRPOUR ROUDBARI, M., SIMSEK, G. & VAN DER ZEE, K.G. 2017 Binary-fluid–solid interaction based on the Navier–Stokes–Cahn–Hilliard equations. In *Fluid Structure Interaction* (ed. S. Frei, B. Holm, T. Richter, T. Wick & H. Yang), Radon Series on Computational and Applied Mathematics, vol. 20, pp. 283–328. De Gruyter.

WOOL, R.P. & O'CONNOR, K.M. 1981 A theory crack healing in polymers. *J. Appl. Phys.* **52** (10), 5953–5963.

XU, Q., WILEN, L.A., JENSEN, K.E., STYLE, R.W. & DUFRESNE, E.R. 2020 Viscoelastic and poroelastic relaxations of soft solid surfaces. *Phys. Rev. Lett.* **125** (23), 238002.

YU, Y.S. 2012 Substrate elastic deformation due to vertical component of liquid-vapor interfacial tension. *Appl. Maths Mech.* **33** (9), 1095–1114.

YU, Y.S. & ZHAO, Y.P. 2009 Elastic deformation of soft membrane with finite thickness induced by a sessile liquid droplet. *J. Colloid Interface Sci.* **339** (2), 489–494.

ZHAO, M., DERVAUX, J., NARITA, T., LEQUEUX, F., LIMAT, L. & ROCHÉ, M. 2018*a* Geometrical control of dissipation during the spreading of liquids on soft solids. *Proc. Natl Acad. Sci. USA* **115** (8), 1748–1753.

ZHAO, M., LEQUEUX, F., NARITA, T., ROCHE, M., LIMAT, L. & DERVAUX, J. 2018*b* Growth and relaxation of a ridge on a soft poroelastic substrate. *Soft Matt.* **14**, 61.

ZHAO, T., WANG, G., HAO, D., CHEN, L., LIU, K. & LIU, M. 2018*c* Macroscopic layered organogel-hydrogel hybrids with controllable wetting and swelling performance. *Adv. Funct. Mater.* **28** (49), 1800793.

ZHENG, B., CHAN, T.S., VAN BRUMMELEN, H. & SNOEIJER, J. 2025 Dynamics of poro-viscoelastic wetting with large swelling [data set]. Zenodo. https://doi.org/10.5281/zenodo.17516418.

ZHENG, B.X. & CHAN, T.S. 2025 Soft wetting ridge rotation in sessile droplets and capillary bridges. *Langmuir* **41** (6), 4146–4153.

ZHENG, B.X., PEDERSEN, C., CARLSON, A. & CHAN, T.S. 2023 Static wetting of a barrel-shaped droplet on a soft-layer-coated fiber. *Soft Matt.* **19**, 8988–8996.

ZHENG, H., CHEN, M., SUN, Y. & ZUO, B. 2022 Self-healing, wet-adhesion silk fibroin conductive hydrogel as a wearable strain sensor for underwater applications. *Chem. Engng J.* **446**, 136931.

VAN ZWIETEN, J.S.B., VAN ZWIETEN, G.J. & HOITINGA, W. 2022 Nutils (7.0). Zenodo. https://doi.org/10.5281/zenodo.6006701.

https://doi.org/10.1017/jfm.2025.10977 Published online by Cambridge University Press